WATER RESOURCES RESEARCH, VOL. 49, 4126–4135, doi:10.1002/wrcr.20324, 2013

A finite volume approach for shallow water flow accounting for high-resolution bathymetry and roughness data

N. D. Volp,[1] B. C. van Prooijen,[1] and G. S. Stelling[1]

Received 25 June 2012; revised 14 May 2013; accepted 18 May 2013; published 16 July 2013.

[1] This study presents a finite volume hydrodynamic model for shallow water flow that computes on a coarse grid, but accounts for high-resolution bathymetry and roughness variations on a subgrid. The detailed information can be incorporated by using the assumption of a uniform flow direction and a uniform friction slope within a part of a coarse-grid cell. It is shown in two examples that the results of coarse-grid simulations become as good as high-resolution results, but at much lower computational cost.

Citation: Volp, N. D., B. C. van Prooijen, and G. S. Stelling (2013), A finite volume approach for shallow water flow accounting for high-resolution bathymetry and roughness data, *Water Resour. Res.*, *49*, 4126–4135, doi:10.1002/wrcr.20324.

1. Introduction

[2] There exists a strong interest in fast and accurate hydrodynamic models. They are used for various purposes, like flood forecasting or to form the basis for morphodynamic models. Both types of simulations need fast models for large domains and at high resolution. Flood forecasting models need to be fast, because such models are to provide results at short notice. Morphodynamic simulations need fast hydrodynamic solvers as the duration of a simulation period is generally long. Nowadays, detailed information of the bathymetry is available due to improved measurement techniques, like LIDAR. Bathymetric data with a very high spatial resolution (of the order of magnitude of meters) can be obtained. The discretization for numerical modeling is still a trade-off between accuracy and computation time. The computation time is generally a limiting factor for the use of high-resolution bathymetry data. Taking into account the high-resolution data on a subgrid would, therefore, be a possible trade-off. There are various methods proposed to incorporate high-resolution bathymetry data as some kind of subgrid: *Sanders et al*. [2008], *Cea and Vázquez-Cendón* [2010], *Bates* [2000], and *Yu and Lane* [2006]. *Casulli* [2009] introduced a subgrid-based hydrodynamic model, accounting for high-resolution bathymetry information in coarse-grid simulations. It is based on the principle that the bed level can vary strongly over short distances, while water levels vary over larger scales. The subgrid method deals with two grids, a coarse computation grid and an underlying subgrid with a higher resolution. The bed level is defined on the subgrid and the water level is assumed to be uniform within a coarse-grid cell. The computations of cell volumes (cell-integrated depth) and cross sections are performed using the high-resolution bathymetry data.

[3] Friction is represented by a nonlinear function of a friction coefficient and velocity. Both can vary strongly over short distances, due to variations in roughness and depth. Coarse-grid simulations use cell averaged depths and velocities, neglecting effects of variations on smaller scale. This causes an overestimation of the friction, which can be illustrated for a simple steady uniform one-dimensional (1-D) flow. For such case, the discharge can be computed analytically using the Chézy equation. The discharge is $Q = WC_z H^{\frac{3}{2}}\sqrt{i_b}$, with: W is the width of channel, C_z is the Chézy coefficient, H is the total depth, and i_b is the bed slope. When the depth in transverse direction is not uniform, for example, when half of the channel has depth H_1 and the other half H_2, the total discharge is given by $Q = \frac{1}{2}WC_z\sqrt{i_b}\left(H_1^{\frac{3}{2}} + H_2^{\frac{3}{2}}\right)$ which is always equal or larger than a discharge based on the average depth: $Q = WC_z\sqrt{i_b}\left(\frac{1}{2}H_1 + \frac{1}{2}H_2\right)^{\frac{3}{2}}$. We elaborate on this in the example of a compound channel in section 3.1. Generally, the friction coefficient is lowered, during the calibration phase, to correct for this underestimation of the conveyance. However, the friction coefficient becomes contaminated with effects of a varying depth and, therefore, becomes grid size dependent. Already in the 1930s, the effect of a varying velocity field on the friction in 1-D models was considered by *Lorentz et al*. [1926] and *Lotter* [1933].

[4] There are numerous options for the spatial discretization of the flow domain. Structured and unstructured grids have both their advantages and disadvantages. For a structured grid, the discretized equations are relatively simple even for anisotropic stresses, but the representation of arbitrary and moving boundaries, for example, due to flooding and drying, is generally a problem. Land-water interfaces vary in type. They can be very sharp, when dealing, for example, with steep dikes or quays. Then, the interfaces do not move in space due to water level variations. In this case, unstructured grids may have an advantage over Cartesian grids. When dealing with tidal flats or river banks with

[1]Department of Hydraulic Engineering, Delft University of Technology, Delft, Netherlands.

Corresponding author: N. D. Volp, Department of Hydraulic Engineering, Delft University of Technology, Stevinweg 1, Delft, NL 2600, Netherlands. (n.d.volp@tudelft.nl)

0043-1397/13/10.1002/wrcr.20324

mildly sloping bottoms the land-water interfaces vary in time. In this case, unstructured grids face similar problems as structured grids. Some classical disadvantages of structured grids compared to unstructured grids have been largely removed by proposing flow solvers that deal with moving and arbitrary boundaries, such as cut-cell methods, immersed boundary methods, quad trees, and so on [*Aftosmis et al*., 1998; *Ye et al*., 1999; *Causon et al*., 2001; *Mittal and Iaccarino*, 2005; *Poretti and De Amicis*, 2011; *Liang and Borthwick*, 2009]. The subgrid method of *Casulli* [2009] offers an elegant algorithm to handle the (moving) boundaries accurately for unstructured grids. This approach combines the advantages of the accurate representation of both sharp and mild land-water interfaces with effectively dealing with the nonlinearity of the continuity equation, due to flooding and drying. This method is also effective for structured grids. Here we use Cartesian grids for simplicity, but the proposed method can also be applied to unstructured grids.

[5] In this paper, we present a finite volume method for shallow water flow. We use a subgrid-based formulation for the continuity (similar to *Casulli* [2009]) and combine it with a subgrid-based momentum conservative scheme for the advection and a subgrid-based formulation for bottom friction. The formulation for bottom friction shows similarities with the effective depth defined in *Defina* [2000] and *Yu and Lane* [2011], but in addition to these studies the spatial variation in roughness is considered too.

[6] Section 2 describes the model formulation based on the shallow water equations, detailing the incorporation of subgrid information in the coarse-grid model. Section 3 shows two numerical steady-state examples. In the first example, the flow in a compound channel is considered. The effect of varying depth and roughness on the flow is isolated. We emphasize the advantage of using local roughness and depth information. The flow in a U-shaped bend is the second example. It shows that a sufficiently refined subgrid can represent both sharp and mild land/water interfaces with satisfactory accuracy. Moreover, the example shows that the flow can be modeled well for a low resolution of the computational grid. The paper is finalized with conclusions and discussions on the applicability and limitations of the method in section 4.

2. Model Description

2.1. Definition of Variables

[7] A subgrid-based, two-dimensional, depth-averaged finite volume model for shallow water is introduced. It accounts for bed level and roughness variations on a smaller scale than the dimensions of a computation cell. The subgrid is a small raster of subgrid cells (pixels) with a surface area of $\delta x \times \delta y = \sigma_{i,j}$ and contains all high-resolution data. The coarse grid has a low resolution compared to the subgrid and is similar to the computation grid of traditional models. It supports coarse-grid variables such as water levels and velocities and the full time integration. In principle, this grid can be of any type, structured, or unstructured. For reasons described in the introduction, we chose for a structured, staggered, Cartesian computation grid. Figure 1a shows a single coarse-grid cell with a non-uniform bed level which is defined on the subgrid. Water levels are defined in the coarse-grid cell centers and velocities at the cell edges. Two types of computation domains are considered. A water level domain has its center at a water level point and is indicated by $\Omega_{m,n}$. A momentum domain has its center at a velocity point in either x direction or y direction, indicated by for instance $\Omega_{m+\frac{1}{2},n}$ and $\Omega_{m,n+\frac{1}{2}}$, respectively (Figure 1b). The subscripts m, n always refer to the location of a coarse-grid variable and the subscripts i, j to variables defined on the subgrid.

[8] The discrete variables are translated from the subgrid or the coarse grid into integrable functions using a simple step function, which is piecewise discontinuous. This so-called indicator function Υ_D is defined for domain D by:

$$\Upsilon_D(x,y,t) = \begin{cases} 1 & (x,y) \in D \\ 0 & (x,y) \notin D \end{cases} \tag{1}$$

[9] The dimensions of domain D can be different for each defined variable and will be specified later. The water level $\zeta(x,y,t)$, at arbitrary location and time, is composed from the coarse grid discrete water levels $\zeta_{m,n}$. Using the indicator function, the water level is defined by:

$$\zeta(x,y,t) = \sum_{m=1}^{M}\sum_{n=1}^{N} \zeta_{m,n}\Upsilon_{\Omega_{m,n}} \tag{2}$$

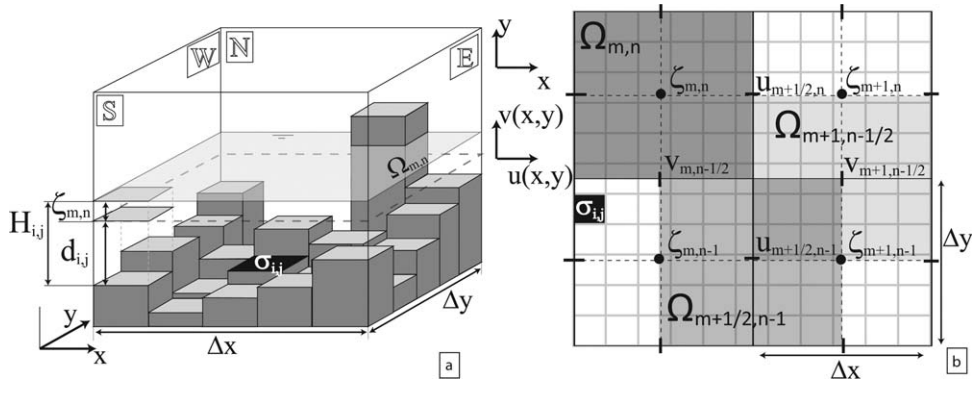

Figure 1. (a) A schematic view of a computation cell with an underlying subgrid, where a part of the domain is dry and (b) an overview of computation cells and domains.

where M and N are the maximum number of coarse-grid cells in x direction and y direction, respectively. The size of domain $\Omega_{m,n}$ ranges from zero to the area of a coarse-grid cell ($\Delta x \times \Delta y$). The exact size of $\Omega_{m,n}$ depends on the wet domain within the cell, that is, the water level and the bathymetry. When parts of the $\Omega_{m,n}$ domain fall dry, its size decreases. The bed level $d(x,y)$, based on bathymetry data, is defined positive in downward direction (Figure 1a) and is defined on subgrid level:

$$d(x,y) = \sum_{i=1}^{I}\sum_{j=1}^{J} d_{i,j}\Upsilon_{P_{i,j}} \tag{3}$$

where I and J are the maximum number of subgrid cells in x direction and y direction and $d_{i,j}$ is the discrete bed level and is defined in the center of a pixel. $P_{i,j}$ is a domain corresponding to a wet pixel with surface area $\sigma_{i,j}$. A domain Ω, related to the coarse grid, contains at least one, but usually multiple subdomains P. Note that the size and number of Ω domains may vary in time. A wet pixel exists when the following condition applies locally:

$$H(x,y,t) = d(x,y) + \zeta(x,y,t) \geq 0 \tag{4}$$

in which H is the water depth. Within a coarse-grid cell (domain $\Omega_{m,n}$) the water level is uniform, but the water depth can vary due to the subgrid scale variation of the bathymetry (see Figure 1a).

[10] Similar to equation (3) the friction coefficient is defined on subgrid level:

$$c_f(x,y) = \sum_{i=1}^{I}\sum_{j=1}^{J} c_{f:i,j}\Upsilon_{P_{i,j}} \tag{5}$$

with $c_{f:i,j}$ the discrete friction coefficient. The friction coefficient can be given by Chézy, Manning, or any other friction formulation. The depth averaged velocity vector $\vec{u}$ consists of the components $u(x,y,t)$ and $v(x,y,t)$. The velocity field is defined by the discrete coarse-grid velocities ($u_{m+\frac{1}{2},n}$ and $v_{m,n+\frac{1}{2}}$) and the indicator function for domain $D = \Omega_{m+\frac{1}{2},n}$ and $D = \Omega_{m,n+\frac{1}{2}}$:

$$\begin{aligned} u(x,y,t) &= \sum_{m=0}^{M}\sum_{n=0}^{N} u_{m+\frac{1}{2},n}\Upsilon_{\Omega_{m+\frac{1}{2},n}} \quad \text{and} \\ v(x,y,t) &= \sum_{m=0}^{M}\sum_{n=0}^{N} v_{m,n+\frac{1}{2}}\Upsilon_{\Omega_{m,n+\frac{1}{2}}} \end{aligned} \tag{6}$$

[11] For convenience later in this paper, the coarse-grid cells are divided into four areas: South-West (SW), South-East (SE), North-West (NW), and North-East (NE), see Figure 2. This division is used for both water level and momentum domains. A similar notation is used to refer to the edges (s) of a cell; North (N), South (S), East (E), and West (W).

2.2. Continuity Equation

[12] The continuity equation reads in finite volume formulation:

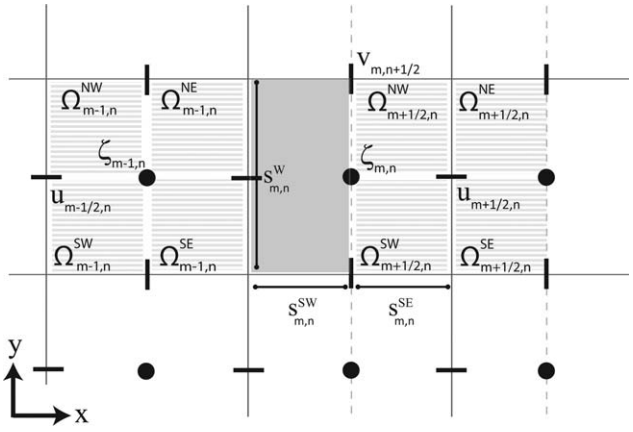

Figure 2. A view of the computation grid including indications of velocity, water level points, and integration boundaries. Also, the subdomains of a water level domain (left) and a momentum domain (right) are indicated as well as the control domain (gray area) used to compute the advection.

$$\left(V_{\Omega_{m,n}}\right)_t = Q^u_{m-\frac{1}{2},n} - Q^u_{m+\frac{1}{2},n} + Q^v_{m,n-\frac{1}{2}} - Q^v_{m,n+\frac{1}{2}} \tag{7}$$

where the subscript t indicates a partial derivative with respect to time, and

$$V_{\Omega_{m,n}}(t) = \iint_{\Omega_{m,n}} H(x,y,t)\mathrm{d}\Omega, \tag{8}$$

[13] Q^u and Q^v are the discharges over the four edges of domain $\Omega_{m,n}$ in u direction and v direction. For example, the discharge at the East side of the cell is defined by:

$$Q^u_{m+\frac{1}{2},n} = u_{m+\frac{1}{2},n}A_{s^E_{m,n}} \tag{9}$$

$$A_{s^E_{m,n}}(t) = \int_{s^E_{m,n}} H(x,y,t)\mathrm{d}y \tag{10}$$

where A_s is the cross-sectional area of edge s.

2.3. Momentum Equation

[14] Inertia, advection of momentum, pressure force, and friction are considered in the momentum balance. This is explained in x direction only, but is similar in y direction:

$$(uV)_t + \tilde{F}^x_{\text{adv}} + \tilde{F}^x_{\text{pres}} + \tilde{F}^x_{\text{fric}} = 0 \tag{11}$$

where $\tilde{F}$ is a force normalized with the density, which is assumed constant. The spatial discretization for each term is described below.

2.3.1. Bottom Friction

[15] In case of gravity-driven shallow-water flow, friction coefficients are often set relatively small, much smaller than would be expected based on the type of bed surface found in the area of the flow. This to correct an overestimation of the friction, due to the neglected effects of small-scale variations in roughness and velocity on the bottom friction as explained in the introduction. By making an estimate of the velocity field on subgrid scale, we want

to account for these variations. The method described below reduces in a 1-D setting to the so-called conveyance method. This method is generally used in 1-D models for the computation of river flow. Early work on this is done by *Lotter* [1933] and *Lorentz et al*. [1926]. Among others, *Chow* [1959] and *Cunge et al*. [1980] give an introduction to this concept. *Yen* [2002] gives an overview of the hydraulic resistance in open channels and also treats various formulations for a resistance coefficient when the depth is nonuniform. In this paper, this concept is generalized for a two-dimensional setting.

[16] Based on the structure of the staggered grid, it is useful to divide the momentum domain in four quarters. First, the friction in a quarter of a cell is derived. The total friction is the sum of the friction of these quarters. The quarter-domain $\Omega^{\mathrm{NE}}_{m,n}$ is taken as an example. The friction is then defined by:

$$\tilde{F}^{x}_{\mathrm{fric}:\Omega^{\mathrm{NE}}_{m,n}} = \iint_{\Omega^{\mathrm{NE}}_{m,n}} c_f |U_p| u_p \mathrm{d}\Omega \qquad \text{with} \qquad |U_p| = \sqrt{u_p^2 + v_p^2} \quad (12)$$

where c_f is the dimensionless friction coefficient as defined in equation (5) and u_p and v_p are the high resolution, depth-averaged velocities in x direction and y direction. These are defined by:

$$u_p(x,y,t) = \sum_{i=1}^{I}\sum_{j=1}^{J} u_{p:i,j}\Upsilon_{p_{i,j}} \quad \text{and} \quad v_p(x,y,t) = \sum_{i=1}^{I}\sum_{j=1}^{J} v_{p:i,j}\Upsilon_{p_{i,j}} \quad (13)$$

where $u_{p:i,j}$ and $v_{p:i,j}$ are the discrete, subgrid velocity components, defined in the center of a pixel. This high-resolution velocity field is constructed in order to account for varying roughness and depth within a momentum domain. However, on subgrid level the spatial variation of the velocity is unknown. A relation between the subgrid velocity field and the coarse-grid velocity field needs to be determined. The first step is to assume a uniform flow direction within a quarter of a momentum domain. This excludes the internal circulations, convergence, and divergence of the flow within this domain. The subgrid velocity is then a linear function of the coarse-grid velocity with a dimensionless factor α_p:

$$u_p = \frac{u}{\alpha_p} \quad \text{and} \quad v_p = \frac{v}{\alpha_p} \qquad \text{for} \quad (x,y) \in \Omega_{m+\frac{1}{2},n} \cap \Omega^{\mathrm{NE}}_{m,n} \quad (14)$$

[17] The friction in domain $\Omega^{\mathrm{NE}}_{m,n}$ can be rewritten to:

$$\tilde{F}^{x}_{\mathrm{fric}_{\Omega^{\mathrm{NE}}_{m,n}}} = u_{m+\frac{1}{2},n}|U^{\mathrm{NE}}_{m,n}| \iint_{\Omega^{\mathrm{NE}}_{m,n}} \frac{c_f}{\alpha_p^2} d\Omega \quad \text{for} \quad (x,y) \in \Omega_{m+\frac{1}{2},n} \cap \Omega^{\mathrm{NE}}_{m,n}$$
$$\text{with } |U^{\mathrm{NE}}_{m,n}| = \sqrt{u^2_{m+\frac{1}{2},n} + v^2_{m,n+\frac{1}{2}}} \quad (15)$$

[18] Note that the absolute velocity is different for each quarter domain. Especially, when parts of the domain are dry, the flow is now not affected by artificial frictional effect of inactive parts in other quarters. Finding a definition for α_p results in a modified friction coefficient that accounts for variations in velocity due to depth and roughness variations within a momentum domain. After assuming a uniform flow direction, the derivation of α_p is performed in streamwise direction. For simplicity, the derivation of the formulation for α_p is shown for a 1-D flow in positive direction. The definition of α_p is, however, independent of the flow direction, as will become clear from equation (18). The coarse-grid velocity within domain $\Omega^{\mathrm{NE}}_{m,n}$ is defined as the volume average of the local subgrid velocities:

$$u = \frac{1}{V_{\Omega^{\mathrm{NE}}_{m,n}}} \iint_{\Omega^{\mathrm{NE}}_{m,n}} H u_p \mathrm{d}\Omega \quad \text{for} \quad (x,y) \in \Omega_{m+\frac{1}{2},n} \cap \Omega^{\mathrm{NE}}_{m,n} \quad (16)$$

The main assumption for defining α_p is assuming a uniform friction slope within domain $\Omega^{\mathrm{NE}}_{m,n}$. The friction slope is the ratio between the water level gradient and the friction term, for positive flow in x direction:

$$S = \frac{c_f u_p^2}{gH} = \text{uniform} \quad \text{for} \quad (x,y) \in \Omega_{m+\frac{1}{2},n} \cap \Omega^{\mathrm{NE}}_{m,n} \quad (17)$$

The friction slope equals the water level gradient and bed slope in case of steady uniform flow. Parameter α_p can now be determined by substituting equation (16) into equation (14) and by writing u_p in terms of the friction slope:

$$\alpha_p = \frac{u}{u_p} = \frac{\frac{1}{V_{\Omega^{\mathrm{NE}}_{m,n}}} \iint_{\Omega^{\mathrm{NE}}_{m,n}} H u_p \mathrm{d}\Omega}{u_p} = \frac{\iint H\sqrt{\frac{SgH}{c_f}}\mathrm{d}\Omega}{\sqrt{\frac{SgH}{c_f}} V_{\Omega^{\mathrm{NE}}_{m,n}}}$$
$$= \sqrt{\frac{c_f}{H}} \frac{1}{V_{\Omega^{\mathrm{NE}}_{m,n}}} \iint_{\Omega^{\mathrm{NE}}_{m,n}} H\sqrt{H/c_f}\mathrm{d}\Omega \quad (18)$$

α_p relates the subgrid and the coarse-grid velocity field. Note that S can be brought outside the integral, as it is assumed uniform within the considered domain. The friction for domain $\Omega^{\mathrm{NE}}_{m,n}$ becomes, after substituting α_p into equation (15):

$$\tilde{F}^{x}_{\mathrm{fric}_{\Omega^{\mathrm{NE}}_{m,n}}} = u_{m+\frac{1}{2},n}|U^{\mathrm{NE}}_{m,n}| \frac{V^3_{\Omega^{\mathrm{NE}}_{m,n}}}{\left[\iint_{\Omega^{\mathrm{NE}}_{m,n}} H\sqrt{H/c_f} d\Omega\right]^2} = \frac{u_{m+\frac{1}{2},n}|U^{\mathrm{NE}}_{m,n}|V_{\Omega^{\mathrm{NE}}_{m,n}}}{H_{f_{\Omega^{\mathrm{NE}}_{m,n}}}} \quad (19)$$

$$\text{using} \qquad H_{f_{\Omega^{\mathrm{NE}}_{m,n}}} = \left[\frac{\iint_{\Omega^{\mathrm{NE}}_{m,n}} H\sqrt{H/c_f}\mathrm{d}\Omega}{V_{\Omega^{\mathrm{NE}}_{m,n}}}\right]^2 \quad (20)$$

where H_f is introduced as the "friction depth." This friction depth is independent of the direction of the flow and can be interpreted as a weighed friction coefficient. It only depends on the subgrid depths and roughness coefficients within the considered domain. The friction depth is

comparable to the "effective depth" described by, for example, *Defina* [2000] or *Yu and Lane* [2011]. However, the friction depth takes variations in depth as well as variations in roughness into account. It also accounts for dry areas within this domain. In the limit of one subgrid cell in a coarse-grid cell, the friction depth reduces to $H_f = \frac{H}{c_f}$.

[19] A momentum domain is covered by four subdomains ($\Omega^{ll}_{m+\frac{1}{2},n}$ with $ll = [\mathrm{NE}, \mathrm{NW}, \mathrm{SE}, \mathrm{SW}]$) each with their local contribution to the friction (equation (19)). The total friction of a u momentum domain becomes:

$$\begin{aligned}\tilde{F}^x_{\mathrm{fric},\Omega_{m+\frac{1}{2},n}} &= u_{m+\frac{1}{2},n} \\ &\left(\frac{|U^{\mathrm{NE}}_{m,n}|V_{\Omega^{\mathrm{NE}}_{m,n}}}{H_{f_{\Omega^{\mathrm{NE}}_{m,n}}}} + \frac{|U^{\mathrm{SE}}_{m,n}|V_{\Omega^{\mathrm{SE}}_{m,n}}}{H_{f_{\Omega^{\mathrm{SE}}_{m,n}}}} + \frac{|U^{\mathrm{NW}}_{m+1,n}|V_{\Omega^{\mathrm{NW}}_{m+1,n}}}{H_{f_{\Omega^{\mathrm{NW}}_{m+1,n}}}} + \frac{|U^{\mathrm{SW}}_{m+1,n}|V_{\Omega^{\mathrm{SW}}_{m+1,n}}}{H_{f_{\Omega^{\mathrm{SW}}_{m+1,n}}}}\right) \\ &= u_{m+\frac{1}{2},n}\sum_{ll=1}^{4}\frac{|U^{ll}|V_{\Omega^{ll}_{m+\frac{1}{2},n}}}{H_{f_{\Omega^{ll}}}} \quad \text{within} \quad \Omega = \Omega_{m+\frac{1}{2},n}\end{aligned} \tag{21}$$

[20] In this way, the effect of small-scale velocity variations on the friction is considered by accounting for high-resolution bathymetry and roughness data.

2.3.2. Pressure Force

[21] The third term of equation (11) is the pressure force. Assuming a hydrostatic pressure gives:

$$\begin{aligned}\tilde{F}^x_{\mathrm{pres}_{\Omega_{m+\frac{1}{2},n}}} &= \iint_{\Omega_{m+\frac{1}{2},n}} H\frac{\mathrm{d}\mathbb{P}}{\mathrm{d}x}\mathrm{d}\Omega \\ &= \iint_{\Omega_{m+\frac{1}{2},n}} gH\frac{\zeta_{m+1,n}-\zeta_{m,n}}{\Delta x}\mathrm{d}\Omega \\ &= g\frac{V_{\Omega_{m+\frac{1}{2},n}}}{\Delta x}\left(\zeta_{m+1,n}-\zeta_{m,n}\right)\end{aligned}$$

where the pressure gradient is assumed to be uniform within a domain $\Omega_{m+\frac{1}{2},n}$.

2.3.3. Inertia and Advection of Momentum

[22] Inertia and advection are given by the first two terms of equation (11). Rewriting these gives:

$$\begin{aligned}(uV)_t + \tilde{F}^x_{\mathrm{adv}} &= u_tV + uV_t + \overline{u}_{s^E}\overline{Q}^u_{s^E} - \overline{u}_{s^W}\overline{Q}^u_{s^W} + \overline{u}_{s^N}\overline{Q}^v_{s^N} \\ &\quad - \overline{u}_{s^S}\overline{Q}^v_{s^S} \quad \text{for} \quad (x,y) \in \Omega_{m+\frac{1}{2},n}\end{aligned} \tag{22}$$

[23] Variables with an over bar, such as $\overline{u}$, indicate a value that is missing at the specific grid location. Subscript s refers to the variable at an edge of the domain $\Omega_{m+\frac{1}{2},n}$, see Figure 2. The last four terms represent the momentum fluxes in and out of domain $\Omega_{m+\frac{1}{2},n}$. Here a momentum conservative scheme for advection is derived, based on *Stelling and Duinmeijer* [2003], *Kramer and Stelling* [2008], and *Kernkamp et al*. [2011]. The missing velocity values are computed by a first-order upwind scheme. Then, only the discharges $\overline{Q}_s$ at the faces of the momentum volume are missing. These are the discharges corresponding to multiple velocity points $\left(\overline{Q}^v_{s^S}, \overline{Q}^v_{s^N}\right)$ and those located at a water level point $\left(\overline{Q}^u_{s^E}, \overline{Q}^u_{s^W}\right)$. When substituting the continuity equation into equation (22), and for simplicity of notation assuming positive flow direction, it can be rewritten as:

$$\begin{aligned}&u_tV + \overline{Q}^u_{s^W}\left(u_{m+\frac{1}{2},n} - u_{m-\frac{1}{2},n}\right) + \overline{Q}^v_{s^S}\left(u_{m+\frac{1}{2},n} - u_{m+\frac{1}{2},n-1}\right) \\ &\quad \text{for} \quad (x,y) \in \Omega_{m+\frac{1}{2},n}\end{aligned} \tag{23}$$

[24] The discharge over a whole face of a water level domain is known based on continuity (equation (9)). However, the distribution of the discharge over a cell face is unknown and can be chosen. A distribution of the discharge over the face based on friction and water depth is used. The unknown discharges $\left(\overline{Q}^u_{s^W} \text{and} \overline{Q}^v_{s^S}\right)$ are based on the discharges at the faces of the subdomains $\Omega^{ll}_{m,n}$ of a water level domain ($ll = \mathrm{SW}, \mathrm{NW}, \mathrm{NE}, \mathrm{SE}$, Figure 2). First, we compute $\overline{Q}^v_{s^S}$ and subsequently $\overline{Q}^u_{s^W}$. This results in the full advection and inertia terms.

[25] In order to find the distribution of the discharge over a face, a subgrid velocity field is constructed. The procedure is similar to the one used for the formulation of the friction term. The construction of the subgrid velocity at face $s^S_{m,n}$ (the face of a water level domain) is used as example. To guarantee continuity, the subgrid velocity field is directly related to the discharge at the face:

$$\begin{aligned}Q^v_s = v_{m,n-\frac{1}{2}}\int_s H\mathrm{d}x = v_{m,n-\frac{1}{2}}A_s = \int_s v_pH\mathrm{d}x \\ \text{with} \quad (x,y) \in s = s^S_{m,n}\end{aligned}$$

Similar to equation (14), the subgrid velocity is a linear function of the coarse-grid velocity, using the dimensionless factor (γ_p):

$$v_{m,n-\frac{1}{2}} = \gamma_p v_p(x,y) \quad \text{with} \quad (x,y) \in s = s^S_{m,n}$$

The discharge over face $s^S_{m,n}$ is then defined by:

$$\begin{aligned}Q^v_{s^S_{m,n}} &= Q^v_{s^{\mathrm{SW}}_{m,n}} + Q^v_{s^{\mathrm{SE}}_{m,n}} = \int_{s^{\mathrm{SW}}_{m,n}} v_pH\mathrm{d}x + \int_{s^{\mathrm{SE}}_{m,n}} v_pH\mathrm{d}x \\ &= v_{m,n-\frac{1}{2}}\left(\int_{s^{\mathrm{SW}}_{m,n}}\frac{H}{\gamma_p}\mathrm{d}x + \int_{s^{\mathrm{SE}}_{m,n}}\frac{H}{\gamma_p}\mathrm{d}x\right).\end{aligned} \tag{24}$$

Similar to equation (17), γ_p is determined by assuming a uniform friction slope (equation (17)). Parameter γ_p and the corresponding friction depth (H_f) are defined in a similar way as for the derivation of α_p:

$$\begin{aligned}\gamma_p &= \sqrt{\frac{c_f}{H}}\frac{\int_{s^{\mathrm{SE,SW}}_{m,n}} H\sqrt{H/c_f}\mathrm{d}x}{A_{s^{\mathrm{SE,SW}}_{m,n}}} \quad \text{and} \\ H_{f_{s^{\mathrm{SE,SW}}_{m,n}}} &= \left[\frac{\int_{s^{\mathrm{SE,SW}}_{m,n}} H\sqrt{H/c_f}\mathrm{d}x}{A_{s^{\mathrm{SE,SW}}_{m,n}}}\right]^2\end{aligned} \tag{25}$$

Considering equation (24) and the definition of the friction depth above, the discharge over a subface $(s^{\mathrm{SE}}_{m,n})$ is:

$$Q^v_{s^{\mathrm{SE}}_{m,n}} = v_{m,n-\frac{1}{2}} \frac{\int_{s^{\mathrm{SE}}_{m,n}} H\sqrt{c_f/H}\,\mathrm{d}x}{\sqrt{H_{f_{s^S_{m,n}}}}} \tag{26}$$

The discharges at other subfaces can be found in a similar way. The discharge $\overline{Q}^v_{s^S_{m+\frac{1}{2},n}}$ is the sum of the discharges over the two subfaces:

$$\overline{Q}^v_{s^S} = Q^v_{s^{\mathrm{SE}}_{m,n-\frac{1}{2}}} + Q^v_{s^{\mathrm{SW}}_{m+1,n-\frac{1}{2}}} \tag{27}$$

Discharge $\overline{Q}^u_{s_{m,n}}$, that is, the discharge through the cell center of a water level domain, is determined by using continuity and the discharge of the subfaces. First, a control volume is composed using the subdomains $\Omega^{\mathrm{NE}}_{m,n}$ and $\Omega^{\mathrm{SE}}_{m,n}$ (gray area in Figure 2). Continuity in this domain implies:

$$\left(V_{\Omega^{\mathrm{NW,SW}}_{m,n}}\right)_t = Q^u_{m-\frac{1}{2},n} - \overline{Q}^u_{s_{m,n}} + \overline{Q}^v_{s^{\mathrm{SE}}_{m,n}} - \overline{Q}^v_{s^{\mathrm{NW}}_{m,n}} \tag{28}$$

The first and second terms are already known, as these are based on values of the previous and the current time step. The two latter terms are determined with the aforementioned method. The discharge at the cell center $\left(\overline{Q}^u_{s_{m,n}}\right)$ follows directly.

[26] The inertia and advective terms from equation (22) are now defined (for positive flow direction) by using equations (24) and (28) by:

$$\begin{aligned} &u_t V + \overline{Q}^u_{s^W}\left(u_{m+\frac{1}{2},n} - u_{m-\frac{1}{2},n}\right) + \overline{Q}^v_{s^S}\left(u_{m+\frac{1}{2},n} - u_{m+\frac{1}{2},n-1}\right) \\ &= u_t V + \mathrm{adv}\,(u) \\ &\mathrm{adv}\left(u_{m+\frac{1}{2},n}\right) = \left(u_{m+\frac{1}{2},n} - u_{m-\frac{1}{2},n}\right)\overline{Q}^u_{s_{m,n}} + \left(u_{m+\frac{1}{2},n} - u_{m-\frac{1}{2},n-1}\right) \\ &\left(\overline{Q}^v_{s^{\mathrm{SE}}_{m,n}} + \overline{Q}^v_{s^{\mathrm{SW}}_{m+1,n}}\right) \quad \text{for} \quad (x,y) \in \Omega_{m+\frac{1}{2},n} \end{aligned} \tag{29}$$

[27] This formulation is momentum conservative and accounts for subgrid scale variations in roughness and depth, including flooding and drying.

2.3.4. Time Integration

[28] In the previous sections, subgrid effects are considered in the evaluation of the momentum and continuity equations. The time integration is semi-implicit for the friction term and fully explicit for the advection. The time step is, therefore, limited by the Courant-Friedrichs-Lewy (CFL) condition based on velocity. This could be avoided by applying a locally implicit method [*Kramer and Stelling*, 2008]. The so-called θ-method is used for the time integration of the advection and gravity term. The time discretization for the continuity and momentum equations results in:

$$\begin{aligned} &\frac{V^{k+1}_{m,n} - V^k_{m,n}}{\Delta t} + u^{k+\theta}_{m+\frac{1}{2},n} A^k_{s^E_{m,n}} - u^{k+\theta}_{m-\frac{1}{2},n} A^k_{s^W_{m,n}} + v^{k+\theta}_{m,n+\frac{1}{2}} A^k_{s^N_{m,n}} \\ &\quad - v^{k+\theta}_{m,n-\frac{1}{2}} A^k_{s^S_{m,n}} = 0 \end{aligned} \tag{30}$$

$$\begin{aligned} &\frac{u^{k+1}_{m+\frac{1}{2},n} - u^k_{m+\frac{1}{2},n}}{\Delta t} + \frac{\mathrm{adv}\left(u^k_{m+\frac{1}{2},n}\right)}{V^k_{\Omega_{m+\frac{1}{2},n}}} + g\frac{\zeta^{k+\theta}_{m+1,n} - \zeta^{k+\theta}_{m,n}}{\Delta x} \\ &\quad + \frac{u^{k+1}_{m+\frac{1}{2},n}}{V^k_{\Omega_{m+\frac{1}{2},n}}} \sum_{ii}^{4} \frac{|U^{ii}_{m+\frac{1}{2},n}|^k V^k_{m+\frac{1}{2},n}}{H^k_{f_{\Omega^{ii}_{m+\frac{1}{2},n}}}} = 0 \end{aligned} \tag{31}$$

The variables at $k+\theta$ are defined by:

$$f^{k+\theta} = (1-\theta)f^k + \theta f^{k+1}$$

[29] In the examples, we use $\theta = 1$ as steady-state solutions are considered. In a subgrid-based model, the volume of a cell is not necessarily a linear function of the water level, as the (wet) cell surface area is a function of the water level as well. An iterative method is needed to solve the system of equations (30). *Casulli* [2009] describes how such a weakly nonlinear system can be solved by means of a Newton iteration. It gives a rigorous proof of the convergence of this method for a sparse system of nonlinear equations. This method is adopted here as well.

3. Examples

3.1. Compound Channel

[30] A compound channel is defined as a channel with a nonuniform cross section. Examples of such systems are rivers with a main channel and flood plains or salt marshes with channels cutting through [*Fagherazzi and Furbish*, 2001]. Especially, the channels on intertidal flats and in salt marshes are relatively small-scale features compared to the size of an estuary. In order to control the computational cost, small-scale bathymetric variations are often not represented well in models covering a large domain. Cross sections and storage capacity are, therefore, often underestimated. In this example, a straight compound channel is considered, emphasizing the effect of a spatially nonuniform friction, due to variations in depth and roughness. We focus on the conveyance of the system. This example is chosen to show the effect of the nonlinearity of the friction term, as was described in the introduction. The dimensions of the compound channel are based on marshes found in the eastern part of the Western Scheldt, at the *Verdronken land van Saeftinghe*. The bathymetry is defined on a subgrid with pixel sizes of 1 m $\times$ 1 m. The computational domain is 63 m wide and 300 m long. The narrow channel is 3 m wide and the bed level is 3 m below the bed level of the flats. The intertidal flats are 30 m wide (Figure 3) and have a higher roughness due to, for example, vegetation. This higher roughness is represented by lower values of the Chézy coefficient. Other formulations for the friction or drag force can be used. Water levels are imposed at the boundaries, forcing the water level gradient equal to the bed slope of 10^{-4}. Nine different water levels are imposed to show the depth dependency. All water levels are within the expected tidal range, see Figure 3. In its steady state, the flow is (almost) uniform in streamwise direction. Differences in results are, therefore, caused by the formulation of the friction term. Three model types are applied to determine the influence of the nonlinear interaction between friction coefficient, velocity, and depth. Table 1 gives an

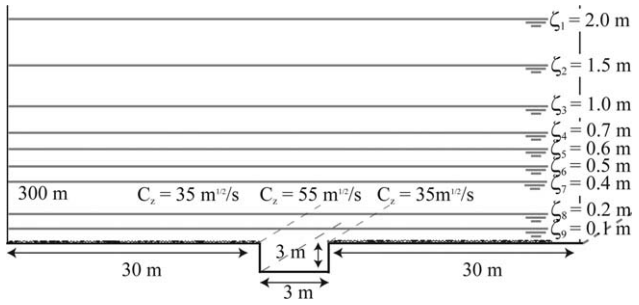

Figure 3. A schematic representation of the compound channel, the flood plains are covered by vegetation, represented by a lower Chézy coefficient. Also the nine different water levels, which serve as boundary conditions for the various simulations are indicated.

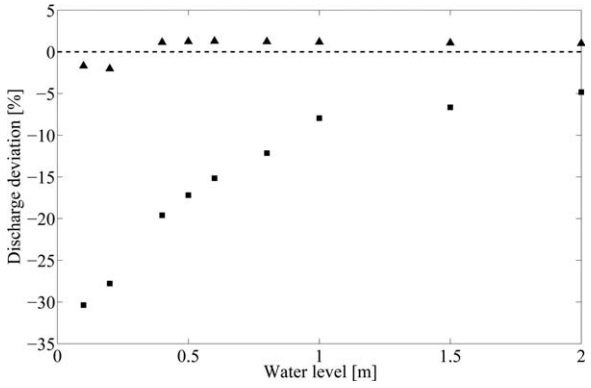

Figure 4. Discharge results for the compound channel example. The relative deviation of the discharge compared to the reference runs (Model A) is plotted for all water levels $\left(\text{Discharge deviation} = \frac{Q_B - Q_A}{Q_A} \times 100\right)$. Results from Model B, subgrid-based continuity equation, are indicated by squares and those of Model C, subgrid-based finite volume approach, with triangles.

overview of the settings of the three models. Model A is the high resolution reference run: The computation grid is equal to the high-resolution subgrid. The results of the two other models are compared to the results of this model. The results of the coarser models (B and C) can in principle not be better than the result of the high-resolution model. The presented method only makes an estimation of the flow on scales smaller than a coarse-grid cell and thus neglects all processes except for friction on that scale. Model A uses the classic formulation for the continuity and momentum equations, as there is no underlying subgrid. Model B is a coarse-grid model that uses a subgrid-based formulation for the continuity equation only. Cross sections and cell volumes are subgrid-based computations, while average values for the velocity and roughness are used in the friction term (the classic approach). Model C uses the full subgrid-based finite volume method, as described in the previous section. Models B and C use a computation grid with only one cell in transverse direction, the computation cell size is 60 m × 63 m. As these two models have only one cell in transverse direction, effectively the flow is simulated in one dimension. Model A simulates the flow in two dimensions, including transverse interactions.

[31] The relative deviation in conveyance (discharge) is shown for the nine different water levels in Figure 4. Model B under predicts the conveyance, especially for low water levels. For these low water levels, the difference in depth between the channel and the flat is relatively large. A uniform bed friction is then a poor representation. The relative difference in depth decreases for higher water levels. A uniform bed friction becomes a more reasonable estimate. The under prediction of the conveyance can be corrected by choosing a lower friction coefficient (c_f). Unfortunately, the correction depends on the grid size and on the water level as shown in Figure 4. This makes a consistent calibration for c_f difficult. The results of Model C are very close to the results of Model A. For all water levels, the deviation is less than 1%. The high-resolution simulations of Model A show a small decrease in water level in the center of the channel. This is due to the dynamic pressure (Bernoulli's Principle), which generates a small exchange of momentum between the channel and the flats. This is not observed in the coarse-grid simulations, as they have only one cell in cross-flow direction. This explains the small deviations found between Models C and A.

[32] We conclude that the computational cost for Models B and C are only a fraction of the time needed to compute the simulation with high resolution (Model A), as follows from the last row in Table 1. This saving in computation time is a consequence of the strong reduction in the number of computation cells. Despite the coarse resolution of the coarse grid, the results for the subgrid-based finite volume method (Model C) are accurate and the error shows no dependence on depth.

Table 1. An Overview of the Three Different Models Performed for the Compound Channel

	Model A	Model B	Model C
Computation cell	1 m × 1 m	60 m × 63 m	60 m × 63 m
Use of subgrid	No	Continuity equation	Full set of equations
Computational cost	100%	0.01%	0.02%

3.2. U-Bend

[33] In the second example, the flow in a U-shaped bend is considered in two dimensions. A depth-averaged simulation is performed, neglecting three-dimensional flow features. We aim to show that the model is capable of simulating flow in a complex geometry with advection effects, similar to cut-cell methods [*Rosatti et al*., 2005]. Figure 5 shows a channel with a deep outer bend, a shallow inner bend, and an overall bed slope of 5.0×10^{-4} in flow direction. The inner radius of the bend is 50 m and the channel width is 100 m. In the lower panel of Figure 5, the cross section of the bed level is plotted at the transects AA' and CC' showing a mild slope in transverse direction. The high-resolution bathymetry is described on 1×1 m^2-sized pixels. The location of the land-water interface at the outer bend is fixed as it is defined as a vertical wall. The location of the land-water boundary at the inner bend depends on the water level and, therefore, on the discharge. For a cut-cell method, it is difficult to locate this inner boundary. The boundary is automatically set in this subgrid-based model,

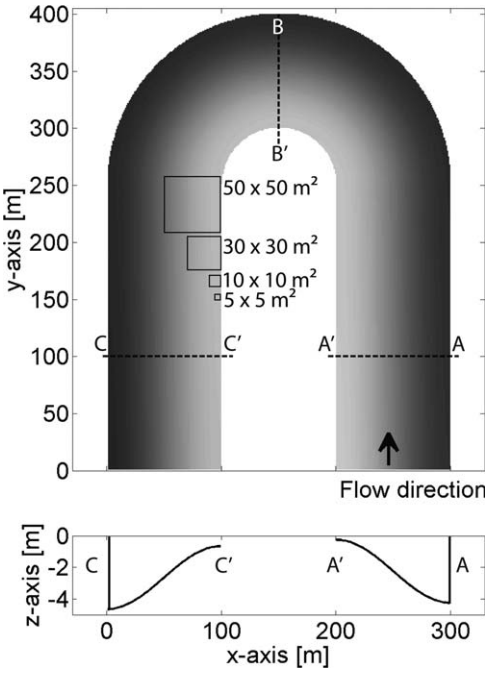

Figure 5. The bathymetry of the U-bend with a deep outer bend and a shallow inner bend. Transects AA', BB', and CC' are used for presenting several results.

because (parts of) coarse-grid cells are allowed to be dry. A constant discharge is imposed at the inflow boundary condition. At the outflow a Neumann boundary is used, imposing the water level gradient equal to the bed slope. These boundary conditions allow the flow to choose its own flow domain within the prescribed bathymetry. A stationary solution is determined for six different discharges ($Q = 30, 50, 80, 100, 120, 300 \mathrm{m}^3/\mathrm{s}$). Four different computation grids with cell sizes of 5×5, 10×10, 30×30, 50×50 m^2 are used. Each simulation is run with and without using the full subgrid method.

[34] The transects AA', BB', and CC' in Figure 5 are defined from the outer bend to the inner bend. Water levels along these transect are plotted in Figure 6 for simulations with subgrid for all different grid sizes. For clarity, only the results of simulations forced with two different discharges are presented. The results for the four cell sizes are plotted with a different color and marking. The results show a minimum grid size dependency. Especially those from the simulations based on the 5×5 m^2 (black line) and 10×10 m^2 (blue, squares) sized grids are almost equal. The error increases slightly for the larger grids (30×30 m^2 (red, open circles) and 50×50 m^2 (yellow, closed circles)). A transverse water level gradient is found in cross-section BB' to create the required centrifugal force. The length of the transects is a measure of the wet domain. This transect increases for higher discharges and is consistent for the various grid sizes. The largest grid sizes are in the same order of magnitude as the width of the flow domain. Only 1–3 cells cover the flow in transverse direction when the channel is not completely submerged. Some flow characteristics can then not be captured anymore. The assumption of a uniform flow direction in a coarse-grid cell is partly violated. However, the results of the larger grids for the higher

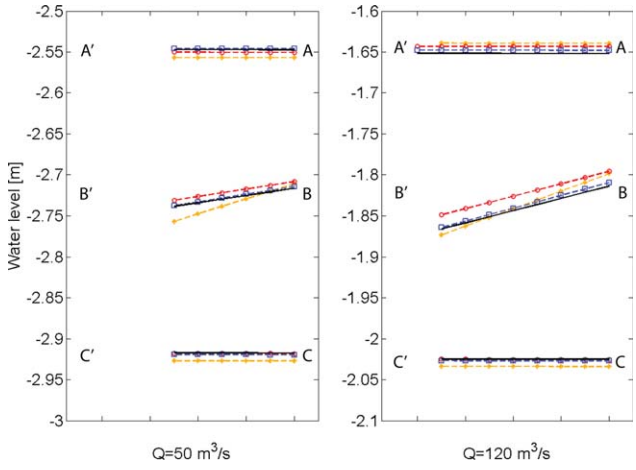

Figure 6. Water level results over three transects for discharges $Q = 50{,}120$ m^3/s, based on simulations with subgrid and computation cells with size 5×5 m^2 (green), 10×10 m^2 (blue), 30×30 m^2 (red), and 50×50 m^2 (yellow).

discharge (right panel of Figure 6) are still in fairly good agreement.

[35] Simulations for various grids and discharges are also performed without using subgrid. The water level results show much larger variations between the grids and only for the two smallest grid sizes, a reasonable result is obtained. Overall, the water level slope in streamwise direction is much larger then the water level slopes found for the subgrid-based simulations. This artificial friction is caused by the discretization, see Figure 7. Note that in this figure the minimum water level in the channel is subtracted from the local water level, showing the relative setup only. The difference between the simulations with and without subgrid is over 40% for the first case (cell size is 10×10 m^2 and $Q = 100$ m^3/s). The setup in water level increases for larger discharges and larger cells, up to 65% (cell size is 30×30 m^2 and $Q = 300$ m^3/s) compared to the higher resolution simulations.

[36] Obviously, the velocity field is less detailed and more patchy when using a low-resolution computation grid. From the streamlines in Figure 8, we can, however, conclude that the bulk flow is modeled correctly with the subgrid model. Various streamlines are drawn starting at

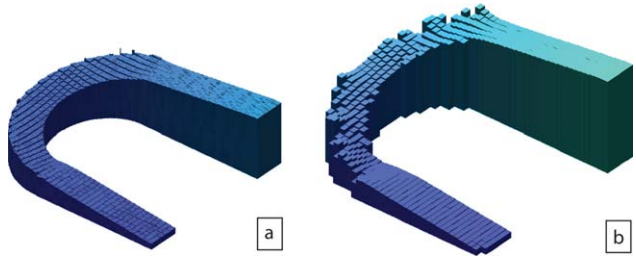

Figure 7. The minimum water level is subtracted from the local water level, this visualizes the increase of water level (setup) in the channel. (a) The first plot is a subgrid-based simulation with a cell size of 10×10 m^2 and a discharge of 100 m^3/s and (b) the second is the counter plot without subgrid.

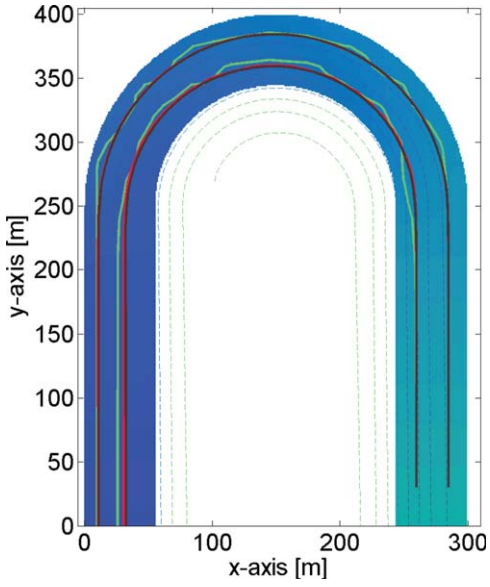

Figure 8. Two sets of three streamlines are drawn for a discharge of 100 m^3/s, based on 5 × 5 m^2 (red), 10 × 10 m^2 (black), and 30 × 30 m^2 (green). The background is the water level and the dashed lines are the depth contours of the full prescribed bathymetry, to indicate the dry area as well.

two different locations using a linear interpolation method within a momentum volume. Results are shown for simulations using a grid size of 5 × 5 m^2 (black), 10 × 10 m^2 (red), 30 × 30 m^2 (green), and $Q = 100$ m^3/s. Although the overall trajectory of the streamlines from the coarse simulations is correct, it is clear that a linear interpolation is used. Especially in the bend, the trajectory of the simulation with the coarsest grid shows deviations that follow from the interpolation.

[37] The computational cost of these simulations with and without subgrid is a only few percent of the cost of the high-resolution simulations. The percentages are similar to the ones found in the previous example. The reduction in computation time is mainly due to the strong reduction in computation cells. With this example of a U-bend, it is shown that the model is capable of representing the correct conveyance of a flow in a complex geometry with advection effects.

4. Discussion and Conclusion

[38] We presented a two-dimensional, finite volume approach for shallow water flow that accounts for high-resolution bathymetry and roughness data. High-resolution effects are considered in coarse-grid computations via a subgrid in both the continuity and the momentum equations. We aimed at increasing the accuracy of two-dimensional, depth-averaged coarse-grid models without a substantial increase in computation time.

[39] To account for the small-scale effects of bathymetry and roughness in formulating the friction and advection terms, a high-resolution velocity field is constructed. The construction is based on two main assumptions. First, we assumed that the flow within a quarter of a cell has a uniform direction and that it scales linearly with the coarse-grid velocity. Internal circulations, convergence, and divergence of the flow are thereby excluded within that domain. Variations in magnitude of velocity on small scale are, however, allowed. This assumption of a uniform flow direction within a cell is made in traditional models as well, but small-scale variations of the magnitude of the velocity field are then excluded too. Second, a uniform friction slope is assumed for the construction of the high-resolution velocity field. This assumption is especially preferred over a uniform velocity for flows in areas with a large variation in bathymetry and/or roughness. In flow domains, where the variation in bathymetry and roughness is small or in domains where the friction is not the dominant process, the assumption of a uniform friction slope is as good as the assumption of a uniform velocity. In summary, the method gives significant improvement of the results in shallow flows with small-scale depth and roughness variations and has no negative effects in other cases.

[40] In theory, the size of the subgrid can be as small as available. The limitations should, however, be kept in mind. The model is based on the depth-averaged shallow water equations. This implies that the flow around three-dimensional roughness elements is not resolved and has to be modeled within the friction coefficient. The minimum size of the subgrid should at least be several times the size of the roughness elements. For example, LIDAR data can have resolutions much smaller than this typical size. It is still a challenge to transform these small-scale features in a roughness coefficient. The size of the coarse grid of the new model is mainly limited by the assumption of a uniform flow direction. If small-scale flow directions have to be resolved, a small coarse grid is required. This limitation is less strict than the limitation of the grid size for traditional models. There, the horizontal scale of the variation in bathymetry and roughness determines the size of the grid cell. This is generally smaller than the size of the circulations or significant deviations in flow direction of interest. The grid size of a coarse grid in a subgrid model simulation can, therefore, be larger than the grid size of a traditional model without loss of accuracy. This results in a strong decrease in computational time.

[41] The presented model offers an improvement of traditional coarse-grid models and captures moving boundaries automatically without any preprocessing. The size of the computational grid is now determined by the spatial scales of the flow direction and much less on the spatial scales of bathymetry and roughness variations. The final result is a strong reduction in computational time, without loss of accuracy.

[42] **Acknowledgments.** The work presented in this paper is carried out as part of the innovation programs Building with Nature and Knowledge for Climate. The Building with Nature program is funded from several sources, including the Subsidieregeling Innovatieketen Water (SIW, Staatscourant 953 and 17009) sponsored by the Dutch Ministry of Transport, Public Works and Water Management and partner contributions of the participants to the Foundation EcoShape. The program receives cofunding from the European Fund for Regional Development EFRO and the Municipality of Dordrecht.

References

Aftosmis, M. J., M. J. Berger, and J. E. Melton (1998), Robust and efficient Cartesian mesh generation for component-based geometry, *AIAA J.*, *36*, 952–960.

Bates, P. D. (2000), Development and testing of a subgrid-scale model for moving-boundary hydrodynamic problems in shallow water, *Hydrol.*

Processes, *14*(11–12), 2073–2088, doi:10.1002/1099-1085(20000815/30)14:11/12 <2073::AID-HYP55 >3.0.CO;2-X.

Casulli, V. (2009), A high-resolution wetting and drying algorithm for free-surface hydrodynamics, *Int. J. Numer. Methods Fluids*, *60*(4), 391–408, doi:10.1002/fld.1896.

Causon, D. M., D. M. Ingram, and C. Mingham (2001), A Cartesian cut cell method for shallow water flows with moving boundaries, *Adv. Water Resour.*, *24*, 899–911.

Cea, L., and M. E. Vázquez-Cendón (2010), Unstructured finite volume discretization of two-dimensional depth-averaged shallow water equations with porosity, *Int. J. Numer. Methods Fluids*, *63*(8), 903–930, doi:10.1002/fld.2107.

Chow, V. T. (1959), *Open-Channel Hydraulics*, pp. 128–132, McGraw-Hill, New York.

Cunge, J. A., F. M. Holly, and A. Verway (1980), *Practical Aspects of Computational River Hydraulics*, pp. 19–23, Pitman, London.

Defina, A. (2000), Two-dimensional shallow flow equations for partially dry areas, *Water Resour. Res.*, *36*(11), 3251–3264.

Fagherazzi, S., and D. J. Furbish (2001), On the shape and widening of salt marsh creeks, *J. Geophys. Res.*, *106*, 911–1003.

Kernkamp, H. W. J., v. A. Dam, G. S. Stelling, and d. E. D. Goede (2011), Efficient scheme for the shallow water equations on unstructured grids with application to the continental shelf, *Ocean Dyn.*, *61*, 1175–1188, doi:10.1007/s10236-011-0423-6.

Kramer, S. C., and G. S. Stelling (2008), A conservative unstructured scheme for rapidly varied flows, *Int. J. Numer. Methods Fluids*, *58*(2), 183–212, doi:10.1002/fld.1722.

Liang, Q., and A. G. L. Borthwick (2009), Adaptive quadtree simulation of shallow flows with wet-dry fronts over complex topography, *Comput. Fluids*, *38*, 221–234, doi:10.1016/j.compfluid.2008.02.008.

Lorentz, H. A., et al. (1926), Verslag Staatscommissie Zuiderzee 1918–1926's (Report of the Government Zuiderzee Commission, only in Dutch available), Gravenhage, Algemene landsdrukkerij.

Lotter, G. K. (1933), Considerations on hydraulic design of channels with different roughness of walls, *Trans. All Union Sci. Res. Inst. Hydraul. Eng.*, *9*, 238–241.

Mittal, R., and G. Iaccarino (2005), Immersed boundary methods, *Annu. Rev. Fluid Mech.*, *37*, 239–261.

Poretti, I., and M. G. M. De Amicis (2011), An approach for flood hazard modelling and mapping in the medium valtellina, *Nat. Hazards Earth Syst. Sci.*, *11*, 1141–1151, doi:10.5194/nhess-11–1141-2011.

Rosatti, G., D. Cesari, and L. Bonaventura (2005), Semi-implicit, semi-Lagrangian modelling for environmental problems on staggered Cartesian grids with cut cells, *J. Comput. Phys.*, *204*(1), 353–377, doi:10.1016/j.jcp.2004.10.013.

Sanders, B. F., J. E. Schubert, and H. A. Gallegos (2008), Integral formulation of shallow-water equations with anisotropic porosity for urban flood modeling, *J. Hydrol.*, *362*(12), 19–38, doi:10.1016/j.jhydrol.2008.08.009.

Stelling, G. S., and S. P. A. Duinmeijer (2003), A staggered conservative scheme for every froude number in rapidly varied shallow water flows, *Int. J. Numer. Methods Fluids*, *43*(12), 1329–1354, doi:10.1002/fld.537.

Ye, T., R. Mittal, H. S. Udaykumar, and W. Shyy (1999), An accurate Cartesian grid method for viscous incompressible flows with complex immersed boundaries, *J. Comput. Phys.*, *156*(2), 209–240, doi:10.1006/jcph.1999.6356.

Yen, B. C. (2002), Open channel flow resistance, *J. Hydraul. Eng.*, *128*(1), 20–39, doi:10.1061/(ASCE)0733-9429(2002)128:1(20).

Yu, D., and S. N. Lane (2006), Urban fluvial flood modelling using a two-dimensional diffusion-wave treatment, part 2: Development of a sub-grid-scale treatment, *Hydrol. Processes*, *20*(7), 1567–1583, doi:10.1002/hyp.5936.

Yu, D., and S. N. Lane (2011), Interactions between subgrid-scale resolution, feature representation and grid-scale resolution in flood inundation modelling, *Hydrol. Processes*, *25*(1), 36–53, doi:10.1002/hyp.7813.